

Nonlocal transport of passive scalars in turbulent penetrative convection

Mark S. Miesch,^{1,2} Axel Brandenburg,^{3,4} and Ellen G. Zweibel²

¹*DAMTP, University of Cambridge, Silver Street, Cambridge CB3 9EW, United Kingdom*

²*JILA, University of Colorado, Boulder, Colorado 80309-0440*

³*Department of Mathematics, University of Newcastle, Newcastle NE1 7RU, United Kingdom*

⁴*NORDITA, Blegdamsvej 17, DK-2100 Copenhagen Ø, Denmark*

(Received 25 May 1999; revised manuscript received 20 September 1999)

We present a Green's function approach for quantifying the transport of a passive scalar (tracer) field in three-dimensional simulations of turbulent convection. Nonlocal, nondiffusive behavior is described by a transilient matrix (the discretized Green's function), whose elements contain the fractional tracer concentrations moving from one subvolume to another as a function of time. The approach was originally developed for and applied to geophysical flows, but here we extend the formalism and apply it in an astrophysical context to three-dimensional simulations of turbulent compressible convection with overshoot into convectively stable bounding regions. We introduce a novel technique to compute this matrix in a single simulation by advecting labeled particles rather than solving the passive scalar equation for a large number of different initial conditions. The transilient matrices thus computed are used as a diagnostic tool to quantitatively describe nonlocal transport via matrix moments and transport coefficients in a generalized, multiorder diffusion equation. Results indicate that transport in both the vertical and horizontal directions is strongly influenced by the presence of coherent velocity structures, generally resembling ballistic advection more than diffusion. The transport of a small fraction of tracer particles deep into the underlying stable region is reasonably efficient, a result which has possible implications for the problem of light-element depletion in late-type stars.

PACS number(s): 47.27.-i

I. INTRODUCTION

The mixing of passive scalars in turbulent fluids is an important problem which occurs in many astrophysical and geophysical settings. The transport of light elements in stars is a prominent example.

In the simplest treatments of mixing, one prescribes a diffusion coefficient which scales with characteristic size l and velocity amplitude v of the turbulence, and is typically much larger than the diffusivity arising from microscopic processes alone. The derivation of the turbulent diffusivity is based, among other things, on the assumption of *locality*, which means that a particle is carried only a very short distance by one eddy before being entrained in a different eddy which is completely uncorrelated with the first.

The local prescription fails if the velocity field displays long range correlations or if the dynamics is governed by broad distribution functions [1]. This is just the situation which is now known to hold in many turbulent flows, including turbulent convection in stars. Recent simulations of convection [2,3] show coherent structures such as strong downward plumes, which extend over several scale heights. The validity of the diffusion approximation must be called into question in such systems. Stull and collaborators [4] have developed an alternative, nonlocal description of turbulent transport based on Green's-function-like constructions called *transilient matrices*, and the approach has been applied to study a variety of atmospheric and oceanic systems through numerical simulations, empirical measurements, and laboratory experiments [4–6]. In this paper we extend this methodology and apply it for the first time to compressible astrophysical flows. In particular, we emphasize the diagnostic capability of transilient matrices and use them to quantita-

tively describe nonlocal transport in numerical simulations of turbulent stellar convection. In the remainder of this introduction we place this approach in context.

A passive scalar field, represented by the particle concentration per unit mass $c(\mathbf{r}, t)$, in a fluid flow $\mathbf{v}(\mathbf{r}, t)$ with negligibly small molecular diffusion (infinite Peclet number) evolves according to the advection equation

$$\frac{\partial c}{\partial t} + \mathbf{v} \cdot \nabla c = 0. \quad (1)$$

(The field is characterized as passive if c does not appear in any of the equations which determine \mathbf{v} .) Equation (1) has the solution

$$c(\mathbf{r}, t) = c(\mathbf{r}_0(\mathbf{r}, t), t_0), \quad (2)$$

where $\mathbf{r}_0(\mathbf{r}, t)$ is the position at some initial time t_0 of a fluid particle which is at position \mathbf{r} at time t . In turbulent flow, the particle paths are so complicated that this exact solution is not usually desired. In practice, all descriptions of turbulent transport are a compromise between the exact description given in Eq. (2) and a tractable simplification of it.

In the local picture, the turbulent diffusion term is the first member of a Taylor series, involving derivatives of c , in which the successive terms are ordered by powers of the mean free path (or correlation length) divided by the size of the system. Turbulent diffusion corresponds to the ∇^2 operator acting on c . Higher order terms have been calculated, for example by Rüdiger [7], who calculated the ∇^4 term for turbulent viscosity and found good agreement with the measured profiles in channel flow. However, the convergence of the series itself is open to question, although in specific ex-

TABLE I. Descriptive summary of the simulations. The convectively unstable layer is always in $0 < z < 1$, and the horizontal extent is always 2 in nondimensional units.

Case	Horizontal resolution	Vertical resolution	Computational domain	Density contrast
1	63	63	$0 \leq z \leq 2$	11
2	126	105	$-0.15 \leq z \leq 1.5$	92

amples such as the related problem of turbulent diffusion in a weakly turbulent medium driven by the Parker instability it was found that the series does converge and that the local approximation is adequate [8].

When the correlation lengths are large, a nonlocal description may be more accurate. The concentration c may be written in terms of a Green's function for the initial value problem

$$c(\mathbf{r}, t, t_0) = \int d\mathbf{r}' G(\mathbf{r}, \mathbf{r}', t, t_0) c(\mathbf{r}', t_0). \quad (3)$$

[The solution (2) can be written in this manner, with the Green's function given by an appropriate δ function.] If the Green's function is sharply peaked about $\mathbf{r} = \mathbf{r}'$ then the local approximation holds. A variety of more general, nonlocal descriptions have been proposed which are often based on integrodifferential or transition-matrix representations of the particle flux (reviewed by [4,9]; see also [10,11]). In particular, Stull and collaborators [4] have suggested a method for computing a discretized analog of the Green's function, which they term the *transilient matrix*, from a numerical simulation of turbulence. A variety of quantitative descriptors of nonlocal, nondiffusive transport can be obtained directly from this matrix once it is computed for a given flow.

In this paper we develop a variant of Stull's technique and apply it to the three dimensional simulations of turbulent stellar convection presented by Brandenburg *et al.* [3]. These are fully compressible, MHD simulations which include overshoot into stable layers above and below the convectively unstable layer. The models employ a rotating cartesian geometry and are tailored to represent the lower parts of the solar convection zone and part of the radiative interior beneath. The boundary conditions in the two horizontal directions are periodic, and the top and bottom boundaries are impenetrable and stress-free. The evolution of the magnetic field is governed by the induction equation with a weak seed initial field. The magnetic diffusivity is small enough so that the amplitude of the field begins to grow exponentially in time (dynamo action). At small and intermediate scales the Lorentz force becomes exceedingly important and leads subsequently to saturation of the dynamo. However, the magnetic energy here is just a few percent of the kinetic energy and there is evidence that such weak fields do not greatly influence the probabilistic properties of the flow such as the local expansion rates of fluid particles and the topological entropy [12].

We consider data from two different simulations, summarized in Table I, that differ mainly in their resolution (63^3 meshpoints in case 1 and $126^2 \times 105$ meshpoints in case 2) and Reynolds numbers (300 and 1200, respectively). The

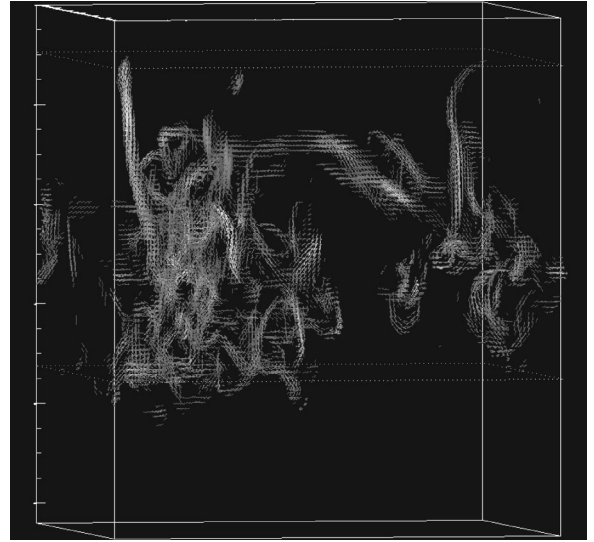


FIG. 1. Shown is a three-dimensional volume rendering of vorticity vectors at a particular timestep in the high-resolution simulation (case 2) in regions where their magnitude exceeds four times the root-mean-square value. The upper and lower overshoot layers are marked by dotted lines. There are two long vortex tubes, associated with plumelike downflow lanes, extending vertically from the top of the convection zone downwards where they merge into a complex vortex tangle just above the lower overshoot layer.

flow in the convection zone is turbulent and exhibits a complex vortical structure, as demonstrated in Fig. 1.

The velocity field appearing in Eq. (1) can either be a fixed snapshot at one particular time in the convection simulations or a dynamic field which is evolved simultaneously according to the full MHD equations. We consider both possibilities, and solve Eq. (1) using lagrangian particles to represent the concentration c .

In the following section, Sec. II, we discuss the transilient matrix method and our implementation of it. In Sec. III we introduce various matrix moments as quantitative descriptors of nonlocal transport and we describe how such moments can be used to derive a series of transport coefficients in a generalized, multiple-order diffusion equation. Throughout the discussion, applications are made to the stellar convection simulations mentioned above, and we summarize the primary results in Sec. IV. A preliminary version of this work has appeared elsewhere [13].

II. THE TRANSILIENT MATRIX

A. Basic formulation

Our goal in this paper is to describe the nonlocal transport of a passive scalar field (i.e., a collection of tracer particles) in simulations of convective turbulence in a manner analogous to Eq. (3). To this end, we can define a discrete version of the Green's function which describes the transport of tracer particles from one subvolume in the computational domain to another as a function of time. Following Stull and collaborators [4], we refer to this discrete analogue of the Green's function as the *transilient matrix* of the flow. Although the system is deterministic, the transilient matrix can be regarded as describing the set of probabilities that a tracer particle originates in one subvolume and ends up in another.

Indeed, in text books on stochastic calculus [14] this is referred to as the conditional probability $P(\mathbf{r}, t | \mathbf{r}', t')$ that a particle at position \mathbf{r}' at time t' ends up at position \mathbf{r} at a later time t . This probability obeys the forward Kolmogorov (or Fokker-Planck) equation

$$\frac{\partial}{\partial t} P(\mathbf{r}, t | \mathbf{r}', t') + \nabla_r \cdot [\mathbf{v}(\mathbf{r}, t) P(\mathbf{r}, t | \mathbf{r}', t')] = 0, \quad (4)$$

where the effect of particle diffusion has been neglected. This equation is identical to the equation for the particle concentration per unit volume. Therefore the Green's function for the concentration per unit mass, is related to P via

$$G(\mathbf{r}, \mathbf{r}', t, t') = \rho^{-1}(\mathbf{r}, t) P(\mathbf{r}, t | \mathbf{r}', t') \rho^{-1}(\mathbf{r}', t'), \quad (5)$$

where ρ is the density of the fluid.

The transilient matrix formalism is similar to other discrete transition matrix approaches (e.g., [10]) and is closely related to many analytical models such as nonlocal generalisations of the more familiar concept of turbulent diffusion, in which the turbulent flux of a passive scalar is assumed to be proportional to gradients in the mean concentration [11]. For comparisons between transilient turbulence theory and other transport models, see [4,15]. However, note that many aspects of these comparisons concern the use of transilient matrices as a turbulent closure model, which we do not in general encourage (see the end of this section).

When considering thermal convection, it is natural to first focus on transport in the vertical (z) direction, parallel to the direction of the gravitational field. We therefore choose our subvolumes to be horizontal layers. As a result, the corresponding transilient matrix will represent the time evolution of the horizontally averaged particle concentration, denoted by $\bar{c}(z, t)$, or rather, its discrete analogue, $\bar{c}_i(t)$, where i denotes a horizontal layer, or bin. Following Eq. (3) we can then express the temporal evolution of the mean concentration per unit mass as

$$\bar{c}_i(t) = \sum_j G_{ij}(t, 0) \bar{c}_j(0), \quad (6)$$

where the subscripts i and j again refer to vertical bins and where we have chosen the origin of our time coordinate to correspond to the instant at which tracer particles are injected. For convenience, we will sometimes refer to the Green's function in continuous space, $G(z, z', t, 0)$, which is approximated by the transilient matrix as

$$G(z_i, z'_j, t, 0) = G_{ij}(t, 0), \quad (7)$$

where z_i and z_j are the depths about which the destination and source bins, i and j , are centered.

The horizontal averaging present in Eqs. (6) and (7) does not compromise the accuracy of the matrices because it is performed *after* the full three-dimensional evolution of the tracer concentration is computed. In other words, $G(z, z', t, 0)$ can only be obtained by computing the evolution of a fully three-dimensional tracer field $c(x, y, z, t)$ for all times between 0 and t . Once computed, the matrix can then be used to calculate the temporal evolution of other initial concentrations with different vertical profiles, provided the

horizontal distribution in all initial tracer fields is uniform within each vertical bin. The prognostic capabilities of transilient matrices and the consequences of horizontal averaging will be discussed in more detail at the end of this section.

In principle, the transilient matrix for a flow can be computed by a series of numerical experiments, each measuring the response of the system to different initial tracer concentrations (usually resembling δ functions). However, this becomes impractical for turbulence simulations because of the computational expense. A more efficient alternative, used by Stull and colleagues [4], is to solve a set of differential equations, each describing the time evolution of a passive scalar field with different δ -function-like initial conditions. We introduce here an even more efficient way of calculating the transilient matrix, G_{ij} , which involves injecting a large number of passive tracer particles, initially uniformly distributed among the levels, advecting them with the flow, and then computing the matrix directly from their statistical behavior. This approach is only valid if microscopic (unresolved) diffusion of the tracer field can be neglected, or in other words, if the associated Peclet number is large. Such an approximation is appropriate for the flows we are considering because they are reasonably turbulent, with momentum and energy transport in general dominated by resolved convective motions. However, it should be kept in mind that large gradients can develop in localized, transient regions of the flow where diffusion can become important and the advective approximation may break down.

In order for the transilient matrix to reflect the evolution of the tracer particle concentration per unit mass, $c(\mathbf{r}, t)$, the ‘‘subvolumes’’ or ‘‘bins’’ used to construct it must each comprise an equal mass of fluid. Thus, the vertical extent of each horizontal layer must systematically decrease as the density increases toward the bottom of the computational domain. Alternatively, bins of equal vertical extent (constant volume) could be used, but the resulting matrix would describe the evolution of the concentration per unit volume, ρc , and it would no longer strictly correspond to the Green's function for equation (1). Note that this was not an issue in previous applications of the transilient matrix technique, which were concerned with Boussinesq fluids [4,5]. Bins of constant mass have been used for the present work except where otherwise noted in Sec. II B. The number of bins to consider is to some extent arbitrary, but here we choose it to be equal to the number of grid points in the vertical direction, so the width of a bin is larger than the grid spacing near the top of the computational domain, where the density is low, and smaller near the bottom.

The temporal evolution of the transilient matrix for one of the simulations (case 2), is exhibited in Figs. 2 and 3. Although the spatial extent of each constant-mass bin increases with depth, the matrices are plotted with respect to z and z' [see Eq. (7)] in order to simplify their physical interpretation and to compare them with analogous matrices obtained using bins of constant volume (see Fig. 5 below). If the mixing occurred via classical diffusion in an infinite domain, cross sections through the matrix would yield Gaussians which would progressively decrease in amplitude and increase in dispersion with time.

Note in the simulations the asymmetric spread away from the diagonal, which is the initial state. Although the peak

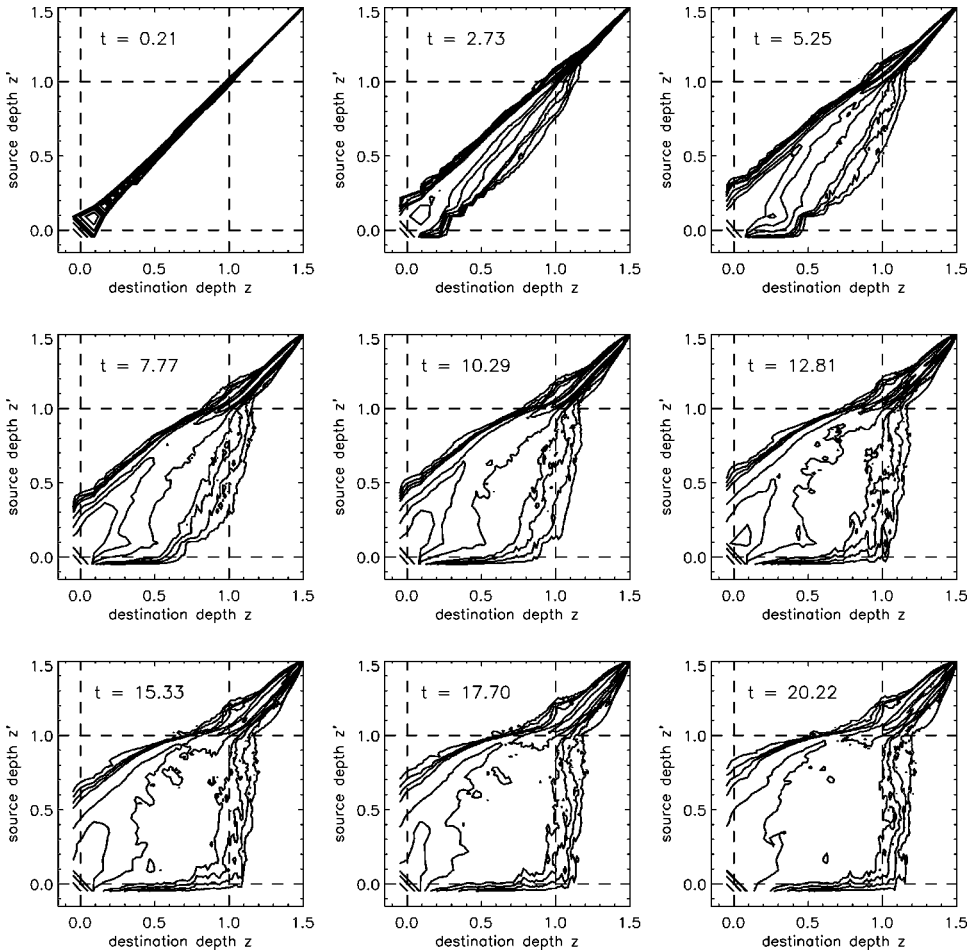


FIG. 2. Shown are contour plots of the evolving transient matrix for case 2 [displayed as $G(z, z', t)$], computed using a fixed velocity field and bins of constant mass. The time corresponding to each frame is indicated (a convective timescale is roughly 20 in dimensionless time units), and dashed lines mark the boundary of the convectively unstable region, which is bounded above and below by regions of stable stratification. The source and destination axes indicate depth, which increases downward, in the direction of the gravitational force. The contour levels are 0.001, 0.003, 0.006, 0.01, 0.03, 0.06, 0.1, 0.3, 0.6, and 1.0.

concentration arising from a source level is typically advected upward, the downward moving particles tend to propagate away from the diagonal more rapidly, reflecting the presence of broad upflows and relatively strong, narrow downflows which are characteristic of turbulent compressible convection (e.g., [16]). This is in stark contrast to numerical simulations and laboratory experiments of atmospheric boundary-layer convection, which generally exhibit narrow upflows and broader, weaker downflows, and the associated transient matrices are skewed in the opposite sense as those presented here [4,6].

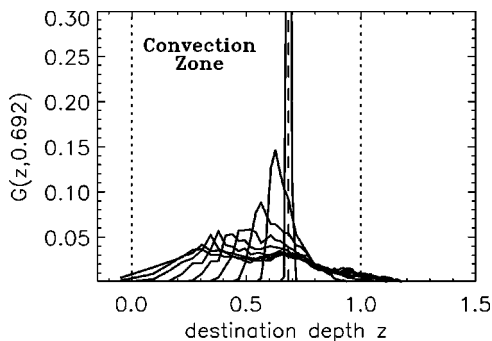


FIG. 3. A cross section through the transient matrix (with bins of constant mass) for case 2 at the same times as in Fig. 1. The concentration begins as a δ function at the source depth, marked with a dotted line, and the progressively more disperse curves correspond to later times. Again, dotted lines mark the boundaries of the convection zone.

The transient matrix, by its nature, must satisfy certain constraints [4]. Among them, G_{ij} must lie between zero and unity, since it is a fractional measure. Also, particle conservation requires that the sum over each column (i.e., over all destinations for a particular source level) equal unity unless tracer particles are allowed to escape the computational domain. If the mass flux, ρv , is divergenceless, and if bins of constant mass are used, then the sum of the matrix elements in each row must also equal unity, provided the tracer particle advection accurately traces the fluid motions. However, in a fully compressible, time-dependent flow this need not be the case and particle accumulation in a given mass bin is possible (note that this statement also applies if a snapshot of the velocity field is used to compute the transient matrix). Figure 4 demonstrates that there is little accumulation on any level for the simulations presented here, with the notable exception of the upper overshoot region in case 2.

We emphasize that although the transient matrices shown in Figs. 2–4 and defined by Eqs. (6) and (7) describe only vertical transport, the full three-dimensional trajectory of each tracer particle is computed for all times. Horizontal averaging is only performed afterward in order to condense the vast amount information contained in the particle trajectories into a more manageable, reduced form represented by the transient matrices.

Still, the horizontal averaging has many implications, particularly concerning the prognostic capabilities of the transient matrix approach. First of all, although Eq. (3) is an exact solution of Eq. (1), Eq. (6) is not the solution of the horizon-

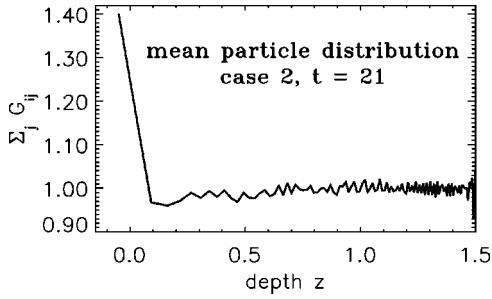


FIG. 4. Shown is the sum over each row of the transient matrix for case 2 at time $t=21$. For uniform initial conditions [$\bar{c}_j(0) = 1$], this is equivalent to the total particle concentration on each destination level, according to Eq. (6).

tal average of Eq. (1), nor is it the horizontal average of Eq. (3) [note that the discretization in Eq. (6) is irrelevant to this conclusion]. The fact that the average Green's function we compute is not a Green's function for the averaged dynamics means that the Green's function cannot in general be "restarted." To illustrate this, consider two times t_1 and t_2 , such that $0 < t_1 < t_2$. According to Eq. (6)

$$\bar{c}_i(t_2) = \sum_j G_{ij}(t_2, 0) \bar{c}_j(0) = \sum_j G_{ij}(t_2, t_1) \bar{c}_j(t_1), \quad (8)$$

where the final equality treats $c_j(t)$ as an initial condition. But, since $\bar{c}_j(t_1) = \sum_k G_{jk}(t_1, 0) \bar{c}_k(0)$, c.f., Eq. (6), we should have

$$G_{ij}(t_2, 0) = \sum_k G_{ik}(t_2, t_1) G_{kj}(t_1, 0). \quad (9)$$

Although Eqs. (8) and (9) hold if the flow is horizontally homogeneous (and if the initial tracer concentration is horizontally homogeneous), this is not in general the case. In fact, Eqs. (8) and (9) are generally not satisfied for our computations. The horizontal averaging represents a loss of information about horizontal particle positions, so if significant horizontal inhomogeneities are present, such as coherent downflow lanes, Eqs. (8) and (9) are no longer satisfied. In this context, it is important to point out that transient matrices do not provide a *prognostic* turbulence closure model in the usual sense, although they have been used for this purpose [4,5]. Instead, transient matrices are in general

most useful as *diagnostic* tools, providing an *a posteriori* description of average properties of the flow. They also provide an efficient way to calculate the temporal evolution of a variety of different (horizontally homogeneous) initial particle concentrations, using simple matrix multiplications rather than full three-dimensional simulations for each initial profile.

B. Variations and extensions

When computing the transient matrix for a dynamical system such as turbulent convection, one has the option of either using a single, time-independent snapshot of the velocity field to advect particles (as in Figs. 2–4) or to continue solving the full fluid equations (or in this case the full MHD equations) and thus evolve the flow in time while the particles are being advected. If the fluid has reached a statistically steady state then the naive expectation is that there will be little difference between the two approaches. However, as pointed out by Vincent, Michaud, and Meneguzzi [17], a "frozen" or "fixed" velocity field can produce too coherent an advection and thus overestimate the transport.

Figure 5 demonstrates that the use of a fixed rather than an evolving velocity field has little influence on the transient matrices computed for the simulations presented here, although there is some indication for slightly enhanced transport in the lower overshoot region and at the upper-ridge-like "advection front." This suggests that the use of a single snapshot in order to mitigate the computational requirements does not significantly alter the results and the subsequent conclusions. In the remainder of this paper, therefore, we present results obtained primarily with fixed velocity fields.

Figure 5 also demonstrates another variation in the way the transient matrix can be defined and computed. The matrix shown in Fig. 5(a) corresponds to the same fixed velocity field as in Figs. 2–4, but was obtained using bins of uniform volume rather than bins of uniform mass. The results are qualitatively similar, although the constant-volume binning strictly describes the evolution of the concentration per unit volume, ρc rather than the concentration per unit mass, c .

A number of more sophisticated three-dimensional binning schemes are also possible, producing a more general Green's function which depends on six spatial dimensions x , y , z , x' , y' , and z' . However, computer memory storage and visualization requirements become prohibitively large at high

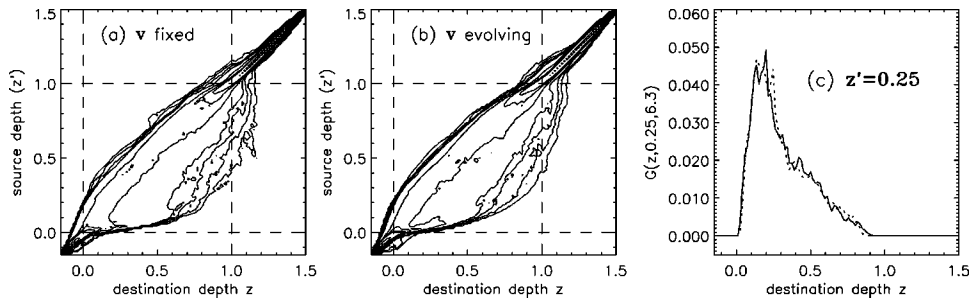


FIG. 5. Two transient matrices are compared, the first computed with respect to a fixed velocity field (a) and the second with respect to a time-evolving velocity field (b), as discussed in the text. The contour levels are the same as those used in Fig. 2. A horizontal cross section of each of these matrices is plotted in panel (c), with the solid and dotted lines denoting the fixed and evolving flow fields, respectively. Both matrices correspond to case 2 at $t=6.3$. Unlike the matrices shown in all other figures, these were obtained using constant-volume bins.

resolutions unless some substantial coarse graining is implemented. Alternatively, we can generalize the approach to study horizontal transport without too much trouble if we simply include the average horizontal particle displacement as an extra dimension—that is, if we consider $G_{vij}(t)$, where ν is the root-mean-square horizontal displacement of a particle which begins on level j and ends up on level i after a time t . In practice, even this reduced matrix can become prohibitively large, so here we select only particular source levels, j , and use a more coarse binning for the destination levels. Results obtained using the G_{vij} matrices will be presented in Sec. III.

An alternative way to describe the time evolution of vertical structures (in a rectangular geometry), which can potentially provide insight into the scale properties of the transport, is by introducing a transilient matrix, or equivalently a Green's function, in Fourier space. For simplicity, we begin with the continuous analogue of Eq. (6):

$$\bar{c}(z,t) = \int G(z,z',t,0)\bar{c}(z',0)dz'. \quad (10)$$

Multiplying Eq. (10) by $\exp(ikz)$, integrating over z , and introducing the equations which define the Fourier transformation:

$$\tilde{c}(k,t) = \int_{-\infty}^{\infty} \bar{c}(z,t)e^{ikz}dz \quad (11)$$

and

$$\bar{c}(z,t) = \int_{-\infty}^{\infty} \tilde{c}(k,t)e^{-ikz}\frac{dk}{2\pi}, \quad (12)$$

we obtain

$$\tilde{c}(k,t) = \int_{-\infty}^{\infty} \tilde{G}(k,k',t)\tilde{c}(k',0)dk', \quad (13)$$

where

$$\tilde{G}(k,k',t,0) = \frac{1}{2\pi} \int_{-\infty}^{\infty} G(z,z',t,0)e^{i(kz-k'z')}dzdz'. \quad (14)$$

Thus, the Green's function describing the evolution of Fourier components through Eq. (13), $\tilde{G}(k,k',t,0)$, is given by applying a Fourier transformation with respect to the destination (first) index of the original Green's function, $G(z,z',t)$, and an inverse transformation with respect to the source (second) index. The real (imaginary) diagonal terms, where $k=k'$, describe the decay of individual cosine (sine) modes, the imaginary (real) diagonal terms describe phase shifts, and the off-diagonal terms, where $k \neq k'$, describe mode mixing.

This spectral approach is most useful when the system to be described is periodic in the dimension which is divided into subvolumes. This is not the case for the present work, which involves binning in the vertical dimension, where the boundaries, the stratification and the transition between con-

vectively stable and unstable regions break the symmetry. We therefore present the method here only for its potential interest.

Finally, it is straightforward to adapt the transilient matrix approach to study the passive advection of vector fields for which the flux through a material area element is conserved. Applications include the transport and amplification of weak magnetic fields in an infinitely conducting medium, which could have relevance for convective dynamos and associated flux transport. Note that in the case of solenoidal fields such as this, it is generally more practical to follow the advection of the corresponding vector potential in order to guarantee the divergence remains zero.

III. APPLICATIONS

A. Matrix moments

Once the transilient matrix is known for a given flow, a number of quantitative measures of nonlocal transport can be obtained from it directly. In this section we consider the moments of the matrix with respect to the destination indices at each source level:

$$M_j^{(n)} = \sum_i (j-i)^n G_{ij}. \quad (15)$$

Analogous moments can also be defined relative to the source indices. We will restrict attention to the mean, variance, and kurtosis, which are the first, second, and normalized fourth-order moments, respectively,

$$\mu_j = M_j^{(1)}, \quad \sigma_j^2 = M_j^{(2)}, \quad \text{and} \quad \kappa_j = M_j^{(4)}/\sigma_j^2. \quad (16)$$

For classical diffusion in an infinite domain, $\mu_j=0$, $\kappa_j=3$, and σ_j^2 increases linearly with time.

Because of the inherent anisotropy of the vertical transport, we generally split the even moments into upward ($i < j$) and downward ($i > j$) components and consider them separately. Furthermore, Eq. (15) can be generalized in a straightforward way to the transilient matrix for horizontal transport, $G_{vij}(t)$ discussed in Sec. II B, to yield moments with respect to the destination shells: $M_{ij}^{(h;n)} = \sum_{\nu} \nu^n G_{vij}$. In what follows, when computing the horizontal moments and similar quantities, we only consider several selected injection levels for particles, i , and for each only consider destination levels within 5 mass bins of the source ($|i-j| \leq 5$), which we then combine to yield a matrix that is in effect only a function of horizontal displacement, ν , source level, i , and time, t .

The destination means for a collection of tracer particles initially uniformly distributed among mass bins are exhibited in Fig. 6 as a function of depth and time for both simulations. The substantial difference in upward and downward transport can be attributed to the effects of density stratification on the velocity field and deep convective penetration into the lower stable region. Large-scale horizontal converging flows near the top of the convection zone sweep particles into strong downflows which persist over several scale heights and transport particles to deeper layers where the more turbulent conditions and less efficient large-scale upward transport make a rapid return trip unlikely. Upward moving par-

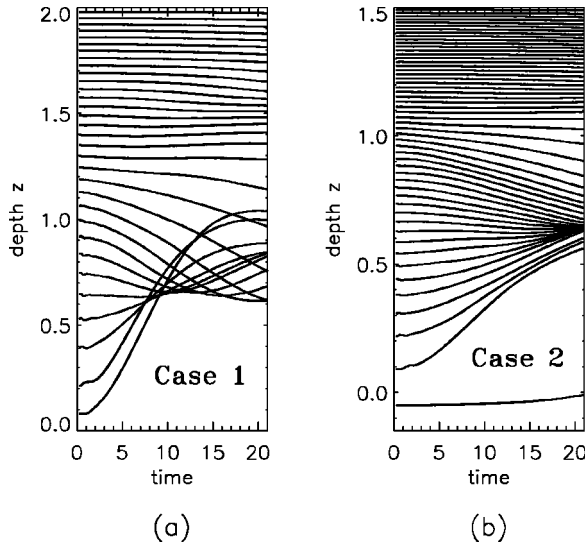


FIG. 6. The mean destination μ_j is shown as a function of source depth and time for (a) case 1 and (b) case 2. The initial ($t = 0$) injection of particles is distributed equally among mass bins (not all bins are displayed). Recall that the convection zone lies in the range $0 \leq z \leq 1$ in both simulations and that a convective turnover timescale is roughly 20 in dimensionless time units.

particles, on the other hand, upon nearing the top of the convection zone, will quickly be swept into strong downdrafts and rapidly reverse direction in roughly half the turnover timescale (depending on their initial height). These tendencies are particularly evident in Fig. 6(a).

The intersecting curves in case 1 suggest large-scale, overturning motions while the more turbulent simulation, case 2, suggests less efficient transport, possibly dominated by more localized, less coherent velocity structures. The mean displacement in case 2 suggests a convergence of particles in the lower convection zone, although Fig. 4 above

indicates that there is no significant accumulation there. The relatively inefficient mixing and particle accumulation in the topmost level in case 2 (Figs. 4 and 6) indicates that once particles are advected into the stably stratified region above the convection zone, they tend to remain there.

The square root of the variance is another measure of the typical particle displacement, or mixing length, measured in mass bins if the transient matrix is so constructed. The upward, downward, and horizontal variances as a function of time at several depths for both simulations are shown in Fig. 7. The axes are logarithmic so the linear behavior over some time intervals apparent in the plots implies a power law relationship of the form $\sigma^2 \sim t^\beta$. A similar power-law behavior is found for most levels, and the value of the best-fit exponents, β , as a function of depth are shown in Fig. 8. The fits typically yield a value close to two, with the notable exception of the vertical transport in upper half of the convection zone.

In many other physical systems as well, the variance is found to scale with time as $\sigma^2 \propto t^\beta$, with $\beta = 1$ corresponding to classical diffusion. A value of β greater than 1 is referred to as superdiffusive or ballistic behavior, while $\beta < 1$ is said to be subdiffusive or stagnant [18]. In practice, the value of β can vary significantly between flows, with turbulent transport being generally superdiffusive. For incompressible, three-dimensional, isotropic, homogeneous turbulence, for example, Richardson’s law predicts $\beta = 3$. Bohr and Pikovsky [20] found moderately superdiffusive behavior, $\beta = 1.38$, for the Kuramoto-Sivashinsky equation, which is a simple, nonlinear field equation exhibiting spatiotemporal chaos. Laminar advection at a constant velocity, from, say, a divergent source, is also superdiffusive, characterized by $\beta = 2$, although laminar convective rolls are subdiffusive, and a value of $\beta = 1/3$ has been predicted and experimentally verified [19]. Lawrence and Schrijver [21] also found subdif-

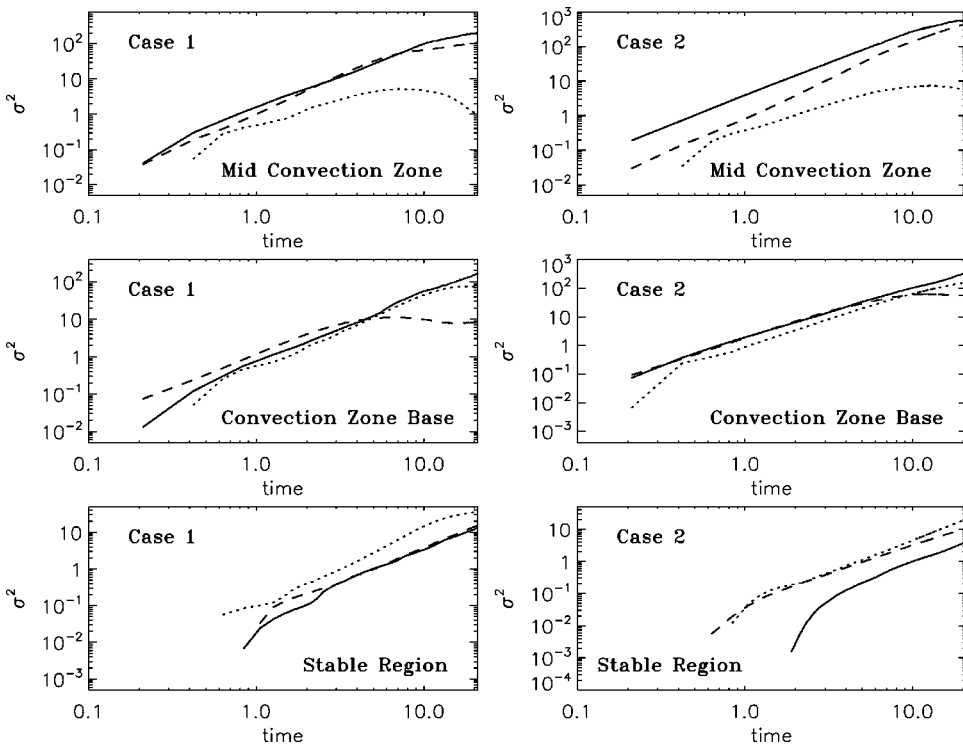


FIG. 7. The upward (dotted lines), downward (dashed lines), and horizontal (solid lines) variances, or mean square particle displacements, are shown for cases 1 and 2 as functions of time at a layer within the convection zone, another in the stable region below it, and another at their interface. The upward and downward variances are the destination moments σ_j^2 , and are measured in mass bins, which become smaller with increasing depth but are comparable to the vertical grid spacing. The horizontal variances are given in terms of the horizontal grid spacing.

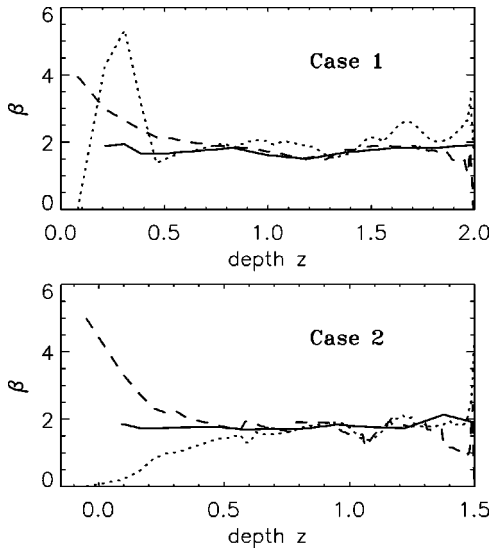


FIG. 8. Best-fit power law exponents which satisfy $\sigma^2 \propto t^\beta$ as a function of depth. A β value of two corresponds to advective behavior, while $\beta=1$ implies classical diffusion.

fusive transport, $\beta \approx 0.89$, for observed magnetic features in the solar photosphere. Our results for the convection simulations presented here indicate superdiffusive transport in both the vertical and horizontal directions, which likely arises primarily from large-scale, coherent flow structures.

The relatively large value of β for the downward variance near the top of the convection zone can be understood if the upper layers are modeled as horizontal flows which converge into downward plumes. To see this, note that the downward variance for a collection of tracer particles is given by

$$\sigma_d^2 = \int_0^\infty \zeta^2 N_p(\zeta, t) \frac{d\zeta}{N_0},$$

where $\zeta = z - z'$, N_0 is the (initial or steady state) number of particles in the source level ($\zeta=0$), and $N_p(\zeta, t)$ is the number of particles located a distance ζ below the source level. For simplicity, we consider a single downward plume with a characteristic, approximately constant velocity w_0 . In this case, $N_p(\zeta, t)$ will vanish for $\zeta > w_0 t$ and will equal $R(t - \zeta/w_0)$ for $\zeta \leq w_0 t$, where $R(t)$ is the rate at which particles enter the downflow at $\zeta=0$. This rate is given by the time derivative of the total number of particles which have entered the downflow after a time t has elapsed, which in turn is given by the (initial or steady state) particle concentration in the source level, c_0 , multiplied by the volume of fluid swept up by each downflow, $\pi(u_0 t)^2 \Delta z$, where u_0 is a typical horizontal velocity scale of the converging flow and Δz is the thickness of the source layer. So, putting this all together, we have, $R(t) = 2\pi u_0^2 \Delta z c_0 t$, and

$$\sigma_d^2(t) = 2\pi u_0^2 \Delta z c_0 \int_0^{w_0 t} \zeta^2 (t - \zeta/w_0) \frac{d\zeta}{N_0} \quad (17)$$

$$= \frac{\pi u_0^2 w_0^3 \Delta z c_0}{6N_0} t^4, \quad (18)$$

which implies a β of 4. The generalization of this result to more than one downward plume yields the same temporal scaling. So, converging flows and downward plumes could be responsible for the increase of β for downward moving particles near the top of the convection zone, where such velocity features may dominate the transport. The small values of β for the upward variance near the top can be attributed to the flattening of the $\sigma^2(t)$ curve as particles reach the top of the convection zone and reverse direction (see Fig. 7).

While the variance provides a measure of the dispersion of the tracer particle distribution function, the kurtosis provides a measure of its shape. The kurtosis values associated with upward, downward, and horizontal transport are exhibited as functions of depth and time in Figs. 9 and 10. Surprisingly, apart from only a few exceptions, the results are largely independent of time. The mid convection zone in case 2, for example, exhibits a kurtosis variation of less than 25% (Fig. 9), over a time interval in which the variances increase by three or four orders of magnitude (Fig. 7). The kurtosis therefore provides a useful quantitative measure for the shape of the transilient matrix as it evolves away from the diagonal. The value $\kappa=3$ is expected for diffusive processes. The larger values exhibited by both simulations, especially for downward transport, point to the importance of high-amplitude displacement events, likely produced by intermittent velocity structures such as strong, localized downward plumes. However, horizontal transport, particularly in the more turbulent simulation, case 2, exhibits kurtosis values closer to 3.

The kurtosis associated with downward transport in both simulations peaks sharply near the base of the convection zone, with less dramatic kurtosis peaks also occurring for upward moving particles in the lower overshoot region. These large kurtosis values imply that penetrative convection can efficiently transport a small fraction of passive tracer particles deep into the underlying stable zone. In late-type stars, such mixing processes are often invoked to explain observed photospheric depletions of Lithium, Beryllium, and other light elements [22]. Most theoretical models of light-element depletion rely on chemical transport during the stars' main sequence lifetimes from their convection envelopes deep into their stable interiors, where light elements are efficiently burned. The results presented here help to support the idea that penetrative convection can provide such a transport mechanism.

B. Generalized diffusion equation

As discussed in the introduction, a common approach to the study of transport in fluids centers around a Taylor expansion of Eq. (3), which yields turbulent diffusion and advection together with terms involving higher order derivatives of the tracer concentration, c . If the correlation length l of the velocity field is small compared to the gradient length scale D of the system, the magnitude of these terms will in general decrease with increasing order as powers of l/D . Even if such a convergence occurs, one must still compute the coefficients of the Taylor expansion up to the order at which they become insignificant.

Transilient matrices contain the information needed to compute such Taylor expansion coefficients, and we now

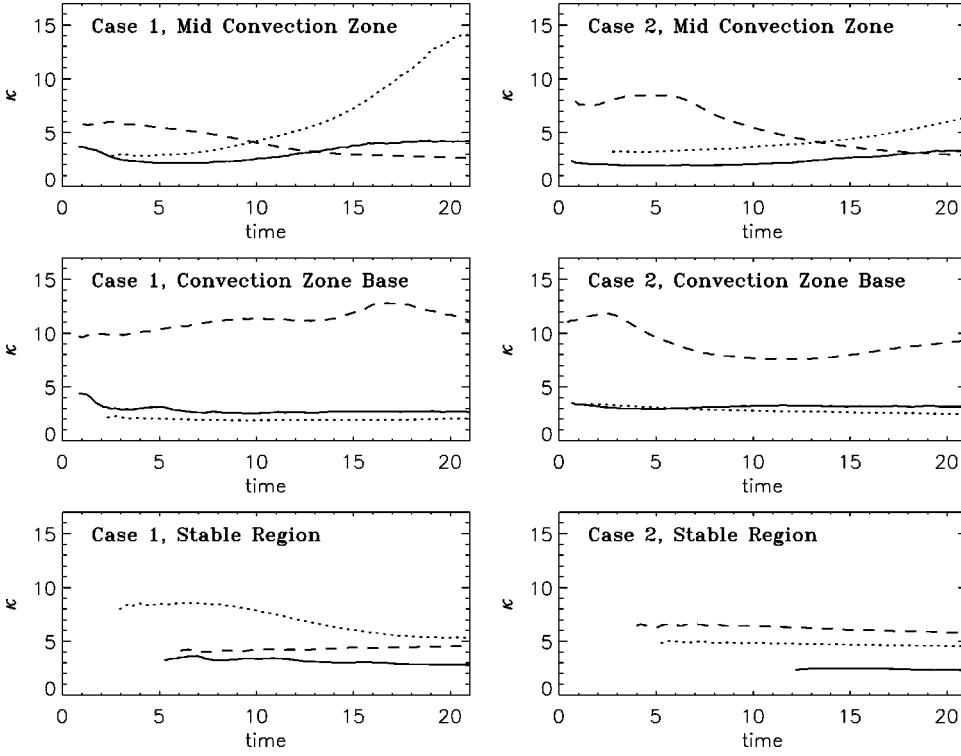


FIG. 9. Shown is the kurtosis in the upward, downward, and horizontal directions, κ , represented, respectively, by dotted, dashed, and solid lines, for cases 1 and 2 at three selected levels in the computational domain. The upward and downward kurtosis values are the destination moments κ_j and are computed with respect to mass bins. The horizontal kurtosis values are computed with respect to the horizontal grid spacing. The artificial cutoffs at early times are imposed because there are initially too few levels populated (<5) to give a reliable result.

proceed to derive them, following a procedure described by Van Beijeren [23]. The first step is to write the Fourier transform of the Green's function [here we use the continuous version, $G(z, z', t) \equiv G(z, z', t, 0)$, for simplicity] as

$$\tilde{G}(k, z', t) = \int e^{-ik\xi} G(\xi, z', t) d\xi = \langle e^{-ik\xi} \rangle, \quad (19)$$

where z' and z are again the source and destination depths [corresponding to levels i and j in the transient matrix; see

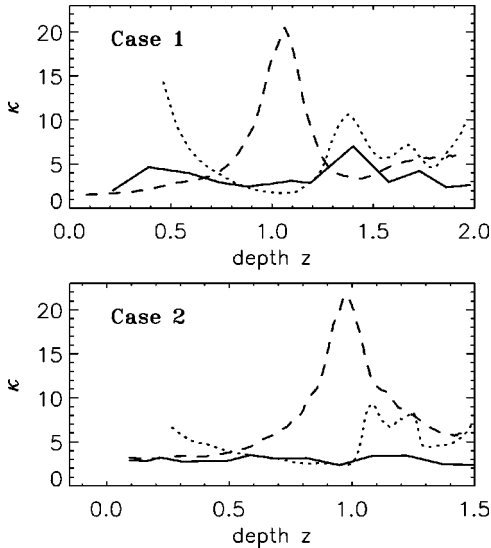


FIG. 10. The kurtosis in the upward (dotted lines), downward (dashed lines), and horizontal (solid lines) directions are shown as a function of depth for cases 1 and 2 at a time $t = 16.8$. The cutoffs for the upward kurtosis near the top of the convection zone and the downward kurtosis near the base are imposed because at levels closer to the boundaries, there are too few data points to give a reliable value.

Eq. (7)], $\xi = z - z'$ and the angular brackets denote an average over all tracer particles. The Green's function can then be expanded in the Taylor series for Eq. (19) and written as follows:

$$\tilde{G}(k, z', t) = \sum_{n=0}^{\infty} \frac{(-ik)^n}{n!} \langle \xi^n \rangle \quad (20)$$

$$= \exp\left(\sum_1^{\infty} \frac{(ik)^n}{n!} \chi_n\right), \quad (21)$$

where the χ_n are cumulative moments, which can be found by equating like powers of k in the two series (20) and (21) [23]:

$$\chi_1 = -\langle \xi \rangle, \quad (22)$$

$$\chi_2 = \langle \xi^2 \rangle - \langle \xi \rangle^2, \quad (23)$$

$$\chi_3 = -\langle \xi^3 \rangle + 3\langle \xi \rangle \langle \xi^2 \rangle - 2\langle \xi \rangle^3, \quad (24)$$

$$\dots \quad (25)$$

Taking a time derivative and applying an inverse Fourier transformation to Eq. (21) then yields

$$\frac{\partial}{\partial t} G(z, z', t) = \sum_{n=1}^{\infty} T_n(z', t) \frac{\partial^n}{\partial z^n} G(z, z', t), \quad (26)$$

where the transport coefficients are given by

$$T_n = \frac{1}{n!} \frac{\partial \chi_n}{\partial t}. \quad (27)$$

Again, in the spirit of the Green's function formalism, an expansion in terms of these transport coefficients yields the

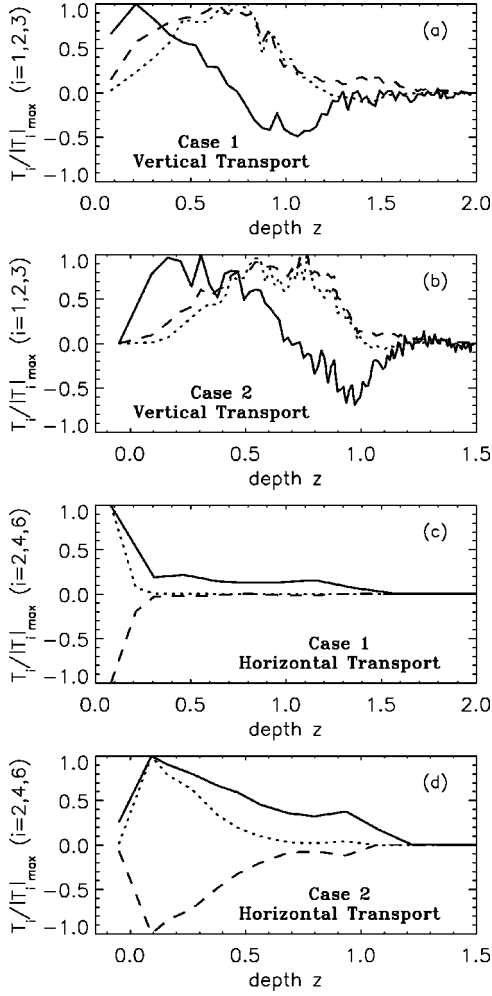


FIG. 11. The transport coefficients T_1 , T_2 , and T_3 (solid, dashed, and dotted lines respectively) describing vertical transport as a function of depth are shown in plots (a) and (b) for cases 1 and 2 at a time $t=3.36$. All are normalized with respect to their maximum magnitudes. Plots (c) and (d) show the normalized values of T_2 , T_4 , and T_6 (solid, dotted, and dashed lines) corresponding to horizontal transport for the same simulations and time.

particle fluxes that would arise in terms of local derivatives of the concentration if the initial concentration were a delta function at level z' . Thus, the time derivative of the concentration for an arbitrary initial condition is again a sum over all the individual contributions:

$$\frac{\partial \bar{c}(z,t)}{\partial t} = \int \sum_{n=1}^{\infty} T_n(z',t) \frac{\partial^n}{\partial z'^n} G(z,z',t) \bar{c}(z',0) dz', \quad (28)$$

and if the T_n are independent of depth, i.e., if the flow is statistically uniform with depth, this reduces to the more familiar, but less general equation,

$$\frac{\partial \bar{c}(z,t)}{\partial t} = \sum_{n=1}^{\infty} T_n(t) \frac{\partial^n}{\partial z^n} \bar{c}(z,t). \quad (29)$$

Whether the transport coefficients can be taken outside the integral or not, the right hand side of Eq. (28) is in the form of the divergence of a generalized flux, as expected for a

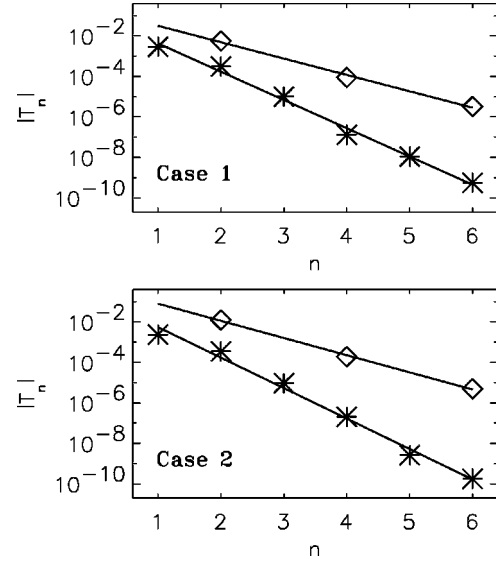


FIG. 12. The magnitude of each transport coefficient, $|T_n|$, is plotted for both simulations as a function of order, n , at time $t=3.36$. Results are averaged over depth and include both vertical (asterisks) and horizontal (diamonds) transport. By construction, the computed horizontal transport coefficients vanish for odd n values.

conservation law. Similar relations also hold for horizontal transport, but note that the assumption of isotropy inherent in our approach implies that the only nonzero horizontal transport coefficients are those with n even.

The first three nonzero transport coefficients in the vertical and horizontal directions for both simulations are exhibited in Fig. 11 as a function of source depth at time $t=3.36$. Note that, for the horizontal transport, only 13 and 14 depths were chosen respectively out of the 63 and 105 available for the two different runs, so the curves are not complete, but do show a definite tendency for the coefficients, especially in case 1, to decrease with depth (with the exception of the uppermost level in case 2, which is located in the relatively quiescent, convectively stable overshoot region). Some decrease in the efficiency of horizontal transport with depth is expected because the characteristic horizontal velocity decreases with increasing density, although this does not explain the more rapid decrease with depth of the higher order coefficients. Note also that the hyperdiffusion (fourth-order) term for horizontal transport is negative in both simulations, corresponding indeed to diffusive as opposed to antidiffusive behavior.

The first-order vertical coefficient can be regarded as a typical advection velocity, and exhibits positive and negative values in the upper and lower regions of the convection zone respectively. The second and third order coefficients peak in the mid to lower convection zone, where vertical mixing is most efficient. The secondary peaks in several of the coefficients just below the interface with the stable region indicate a typical scale at which downward plumes penetrate, diverge horizontally, then reverse direction due to buoyancy forces and transport particles back upward.

The magnitudes of the transport coefficients, $|T_n|$, averaged over depth for the same times as shown in Fig. 11, are plotted in Fig. 12 as a function of order, n . For both vertical and horizontal transport, the expansion of Eq. (28) is found to converge exponentially with increasing n . The relative

dominance of the T_1 coefficient indicates that the vertical transport is more advective than diffusive, which is consistent with Fig. 8 above.

IV. CONCLUSION

In this paper, we have extended the transilient matrix technique [4,5] for describing nonlocal transport and have applied it to simulations of turbulent compressible convection in stellar interiors. We have emphasized the diagnostic capability of the approach, although we also demonstrate that the transilient matrix cannot be applied recursively, which limits its utility as a prognostic turbulence closure model.

We have found little difference in the results obtained using fixed or time-evolving velocity fields, which suggests that the flow's transport properties are governed by its spatial complexity, and that temporal changes are comparatively unimportant. There are examples of other flows where this is not the case. Turbulent shear flows in rotating astrophysical discs, for instance, show strong converging flow regions which can lead to persistent particle accumulation, but time evolving simulations show that the patterns evolve before particles have a chance to accumulate [24].

In both simulations considered, the turbulent transport is found to be nonlocal, anisotropic, and more advective than diffusive. Transport coefficients in a generalized, nonlocal

diffusion equation are found to converge exponentially with increasing order of the differentiation (Fig. 12). The advective nature of transport in the convection zone can likely be attributed to coherent flow structures such as downward-directed vertical plumes and converging horizontal flows, which lead to ballistic particle trajectories. Advective transport in the convectively stable layer could be due to overshooting downward plumes and particle trapping in gravity waves [25].

The destination kurtosis as a function of source depth provides a useful measure of how the tracer particles disperse. For horizontal transport, it is ≈ 3 , but for vertical transport it is generally larger and more depth-dependent. Both simulations exhibit a sharp peak in the kurtosis associated with downward transport near the base of the convection zone, which may have implications for light-element depletion in stars with convective envelopes (Sec. III A).

ACKNOWLEDGMENTS

This work was supported in part by the NASA Sun-Earth Connection program, by the NSF Grant No. AST-9521779, by the Advanced Study Program at NCAR, and by the PPARC Grant No. GR/L 30268. We are happy to acknowledge useful discussions with Juri Toomre.

-
- [1] Reviewed by J.-P. Bouchaud and A. Georges, *Phys. Rep.* **195**, 127 (1990).
- [2] E.g., F. Cattaneo, N.H. Brummell, J. Toomre, A. Malagoli, and N.E. Hurlburt, *Astrophys. J.* **370**, 282 (1991); N.H. Brummell, N.E. Hurlburt, and J. Toomre, *ibid.* **473**, 494 (1996).
- [3] A. Brandenburg, R.L. Jennings, A. Nordlund, M. Rieutord, R.F. Stein, and I. Tuominen, *J. Fluid Mech.* **306**, 325 (1996).
- [4] R.B. Stull, *J. Atmos. Sci.* **41**, 3351 (1984); E.E. Ebert, U. Schumann, and R.B. Stull, *ibid.* **46**, 2178 (1989); R.B. Stull, *Boundary-Layer Meteorol.* **62**, 21 (1993).
- [5] R.B. Stull and E.B. Kraus, *J. Geophys. Res. [Oceans]* **92**, 10 745 (1987); R.B. Stull and A.G.M. Driedonks, *Boundary-Layer Meteorol.* **40**, 209 (1987); W.H. Raymond and R.B. Stull, *Mon. Weather Rev.* **118**, 2471 (1990); M.G. Inclin, R. Forkel, R. Dlugi, and R.B. Stull, *Boundary-Layer Meteorol.* **79**, 315 (1996).
- [6] A. Cenedese and G. Querzoli, *Meas. Sci. Technol.* **8**, 1553 (1997).
- [7] G. Rüdiger, *ZAMM* **62**, 95 (1982).
- [8] K.-H. Hasler, M. Kaisig, and G. Rüdiger, *Astron. Astrophys.* **295**, 245 (1995).
- [9] P.G. Georgopoulos and J.H. Seinfeld, *Chem. Eng. Sci.* **44**, 1995 (1989).
- [10] B.H. Fiedler, *J. Atmos. Sci.* **41**, 674 (1984); B.H. Fiedler and C.-H. Moeng, *ibid.* **42**, 359 (1985); J.E. Pleim and J.S. Chang, *Atmos. Environ., Part A* **26A**, 965 (1992).
- [11] R. Berkowicz and L.P. Prahm, *J. Fluid Mech.* **100**, 433 (1980); F. Hamba, *J. Atmos. Sci.* **52**, 1084 (1995).
- [12] A. Brandenburg, I. Klapper, and J. Kurths, *Phys. Rev. E* **52**, R4602 (1995).
- [13] M.S. Miesch, A. Brandenburg, E.G. Zweibel, and J. Toomre, *Proceedings of the Fourth SOHO Workshop: Helioseismology* (ESA, Noordwijk, 1995), Vol. 2, p. 253.
- [14] E.g., N.G. van Kampen, *Stochastic Processes in Physics and Chemistry* (North-Holland, Amsterdam, 1981); C.W. Gardiner, *Handbook of Stochastic Methods* (Springer, Berlin, 1983).
- [15] G. Chrobok, S. Raasch, and D. Etling, *Boundary-Layer Meteorol.* **58**, 69 (1992); J. Cuxart, P. Bougeault, P. Lacarrere, J. Noilhan, and M.R. Soler, *Boundary-Layer Meteorol.* **67**, 251 (1994).
- [16] F. Cattaneo, N.H. Brummell, J. Toomre, A. Malagoli, and N.E. Hurlburt, *Astrophys. J.* **370**, 282 (1991).
- [17] A. Vincent, G. Michaud, and M. Meneguzzi, *Phys. Fluids* **8**, 1312 (1996).
- [18] E.g., X.-J. Wang and C.-K. Hu, *Phys. Rev. E* **48**, 728 (1993).
- [19] O. Cardoso and P. Tabeling, *Europhys. Lett.* **7**, 225 (1988); Y. Pomeau, A. Pumir, and W.R. Young, *Phys. Fluids A* **1**, 462 (1989); E. Knobloch and W.J. Merryfield, *Astrophys. J.* **401**, 196 (1992).
- [20] T. Bohr and A. Pikovsky, *Phys. Rev. Lett.* **70**, 2892 (1993).
- [21] J.K. Lawrence and C.J. Schrijver, *Astrophys. J. Lett.* **411**, 402 (1993).
- [22] E. Schatzmann and A. Baglin, *Astron. Astrophys.* **249**, 125 (1991); J.-P. Zahn, *Space Sci. Rev.* **66**, 285 (1993).
- [23] H. Van Beijeren, *Rev. Mod. Phys.* **54**, 196 (1982).
- [24] L.S. Hodgson and A. Brandenburg, *Astron. Astrophys.* **281**, 421 (1998).
- [25] E. Schatzmann, *Astron. Astrophys.* **279**, 431 (1993); J. Montalbán, *ibid.* **281**, 421 (1994).